Arabian Journal of Chemistry 16 (2023) 105342

Contents lists available at ScienceDirect

Arabian Journal of Chemistry

journal homepage: www.sciencedirect.com

Original article

Eco-friendly auto-combustion synthesis and characterization of $SmMnO_3/Sm_2O_3/Mn_2O_3$ nanocomposites in the presence of saccharides and their application as photocatalyst for degradation of water-soluble organic pollutants

Mina Jamdar [a], Zahra Heydariyan [a], Asaad H. Alzaidy [b], Elmuez A. Dawi [c], Masoud Salavati-Niasari [a,*]

[a] Institute of Nano Science and Nano Technology, University of Kashan, Kashan, P.O. Box. 87317-51167, Islamic Republic of Iran
[b] Department of Laboratory and Clinical Science, College of Pharmacy, University of Al-Qadisiyah, Diwaniyah, Iraq
[c] Nonlinear Dynamic Research Center (NDRC), College of Humanities and Sciences, Ajman University, P.O. Box 346, Ajman, United Arab Emirates

ARTICLE INFO

Article history:
Received 4 June 2023
Accepted 7 October 2023
Available online 11 October 2023

Keywords:
$SmMnO_3/Sm_2O_3/Mn_2O_3$ nanocomposites
Perovskites
Auto-combustion synthesis
Saccharides
UV-light-driven photocatalysis

ABSTRACT

Organic dyes as major effluents from a variety of industries have been introduced as unwanted pollutions of the environment. In this study, UV-light-driven $SmMnO_3/Sm_2O_3/Mn_2O_3$ nanocomposites were fabricated through eco-friendly carbohydrate sugars-based auto-combustion route. A number of different saccharides were selected as both fuel and capping agent to detect the uniformity, structure, morphology, and dimension of the products. Successful realization of field emission scanning electron microscopy (FE-SEM) and transmission electron microscopy (TEM) analyses over the samples showed that the presence of maltose can provide a morphologically desirable sample. To have the best photocatalytic ability of the $SmMnO_3/Sm_2O_3/Mn_2O_3$ nanocomposites, the degradation rate of simulation wastewaters containing Rhodamine B (RhB), Erythrosine (EY), Methyl violet (MV) and Methyl orange (MO) in 10 ppm was investigated under UV light. Considering MO as suitable pollutant model, the highest efficiency was obtained to be 72.24% for samples synthesized in the presence of maltose. The dye-degradation mechanism confirmed the h^+, and $^{\bullet}O_2^-$ as key species involved in photo-reaction. These compounds were also detected to be reusable.

1. Introduction

In general, population growth with the advancement of different industries has led to the release of wastewater including harmful and damaging pollutants such as chemical dyes and phenolic compounds into the environment (Sajadi et al., 2020; Verma et al., 2022; Yadav et al., 2022). Since these organic components have little biodegradability, the discharge of wastewater containing toxic organic pollutants such as Erythrosine (Honarmand et al., 2020), Methylene blue, Eriochrome lack T, Acid red 14 (Sadegh et al., 2020), Methyl Orange, Malachite Green and Rhodamine B (Ji et al., 2021) leads to harmful effects on the environment and person life (Verma et al., 2023). Therefore, it is generally accepted that a dye is the primary factor of pollutants that are challenging to analyze (Yadav et al., 2022). Among a number of techniques, photocatalysis has gained enormous popularity in terms of the elimination of harmful pollutants like dyes (Piao et al., 2021; Zhang et al., 2019a; Zinatloo-Ajabshir and Mousavi-Kamazani, 2021). In this manner, with the rising interest into the removal of hazardous pollutants, the development of semiconductor-based heterogeneous catalysts have gained considerable attention to initiate photocatalytic performance (Wu et al., 2019). Perovskites type oxides, $AMnO_3$, has been recently used owing to their unique properties, including ferroelectricity, magneto-resistance, and, multiferroicity (Romaguera-Barcelay et al., 2021). Perovskites, especially $REMnO_3$ (RE = rare-earth ions) has been accepted in a variety of applications such as gas sensors (Zhang et al., 2019b), solid oxide fuel cells (Paul et al., 2023), lithium-ion batteries (Yue et al., 2019), photocatalysts (Xing et al., 2021), and magnetic memory devices (Gadani et al., 2017).

* Corresponding author.
E-mail address: salavati@kashanu.ac.ir (M. Salavati-Niasari).

Peer review under responsibility of King Saud University.

Production and hosting by Elsevier

https://doi.org/10.1016/j.arabjc.2023.105342
1878-5352/

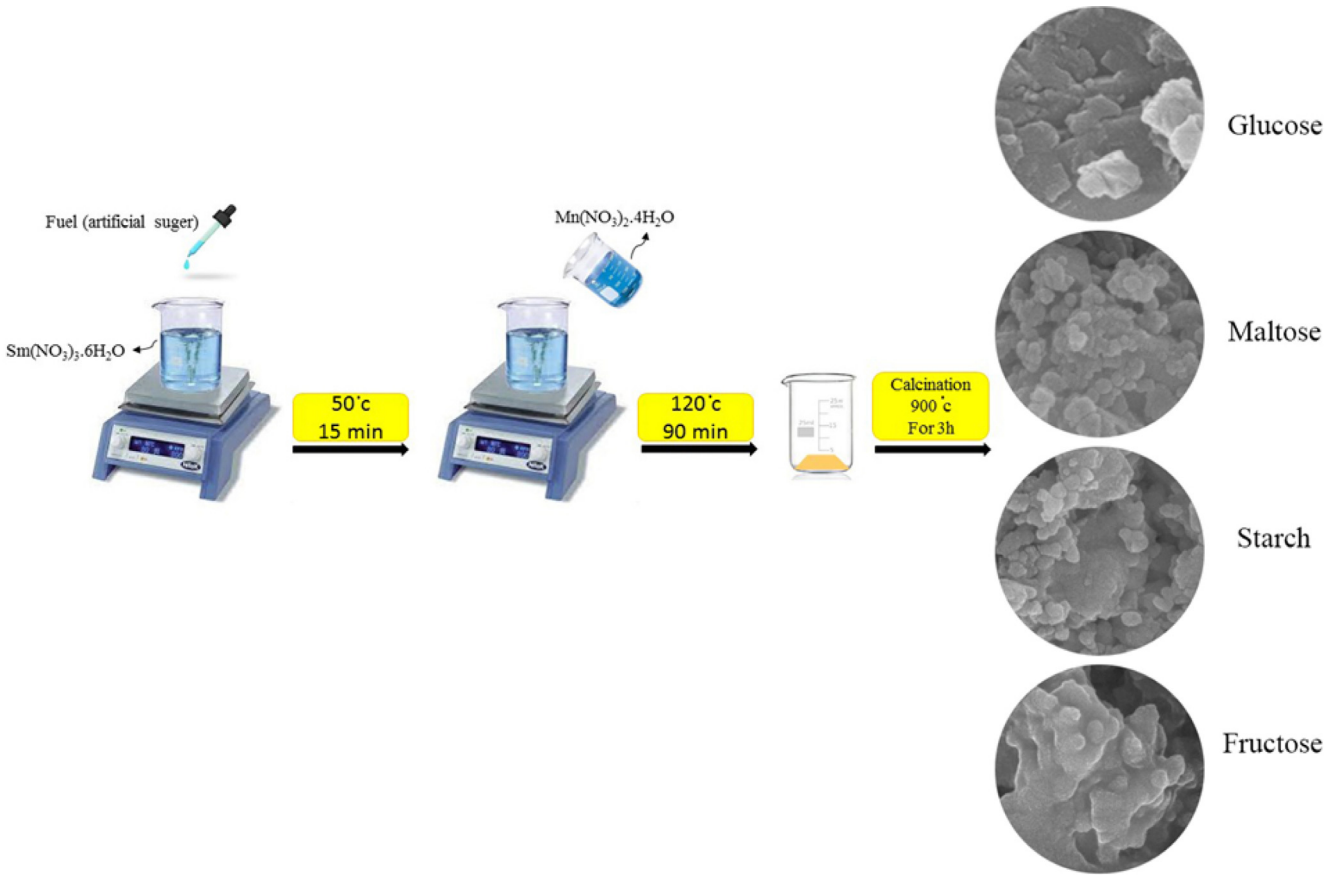

Scheme 1. Schematic process of combustion synthesized Sm-Mn-O-based nanostructures in the presence of different carbohydrate sugars.

Table 1
Preparation conditions for Sm-Mn-O nanostructures.

Sample No.	Types of sugar	Average Crystallite size/XRD (nm)
1	Glucose	21.08
2	Fructose	22.08
3	Maltose	10.79
4	Starch	14.34

The characteristics of this family are due to a stable combination of tunable crystal structures, oxygen mobility, redox behavior, and many more (Luo et al., 2019; Wahba et al., 2022). Among them, samarium manganite-based compounds ($SmMnO_3$) hold the advantages of its unique structure and good catalytic performance in recent years. Unfortunately, it should be noted that the deep study on the photocatalysis performance of the $SmMnO_3$ structures has not been widely reported yet. Although, the needs for the examination of the photocatalytic degradation of organic pollutions over these compounds is necessary, designing $SmMnO_3$-based heterojunctions can exposes more active sites and develop the chemical reaction activity *via* the charge transfer characteristics. To the best of our knowledge, ternary $SmMnO_3/Sm_2O_3/Mn_2O_3$ nanocomposites will be prepared by auto-combustion route using different carbohydrate sugars as fuel and capping agent for the first time. The spectroscopic and technological characterizations of composite samples have been evaluated by employing a series of analyses, such as XRD, SEM, EDS, FT-IR, TEM, BET, and DRS. Further, the synergistic effect between three distinct components and the possible mechanisms of the $SmMnO_3$/

Table 2
A comparison study on the photodegradation efficiency of different perovskite structures under UV light.

Photocatalyst	Method	Targeted Pollutants	Photodegradation time	Percentage%	Ref.
$LaMnO_3$	sol–gel combustion	MO	36 h	76%	(Li et al., 2009)
$YMnO_3$	Hydrothermal	MO	6 h	64.3%	(Kumar et al., 2019)
$TbMnO_3$	hydrothermal	MO	6 h	69.3%	(Kumar et al., 2017)
$DyCoO_3$	solution-polymerization	MG*	2 h	47%	(Michel et al., 2019)
$TbFeO_3$	sonication	MO	2 h	40 ± 0.5	(Mehdizadeh et al., 2020)
$SmMnO_3/Sm_2O_3/Mn_2O_3$	sol–gel combustion	MO	2 h	72.24%	This work

*Malachite Green.

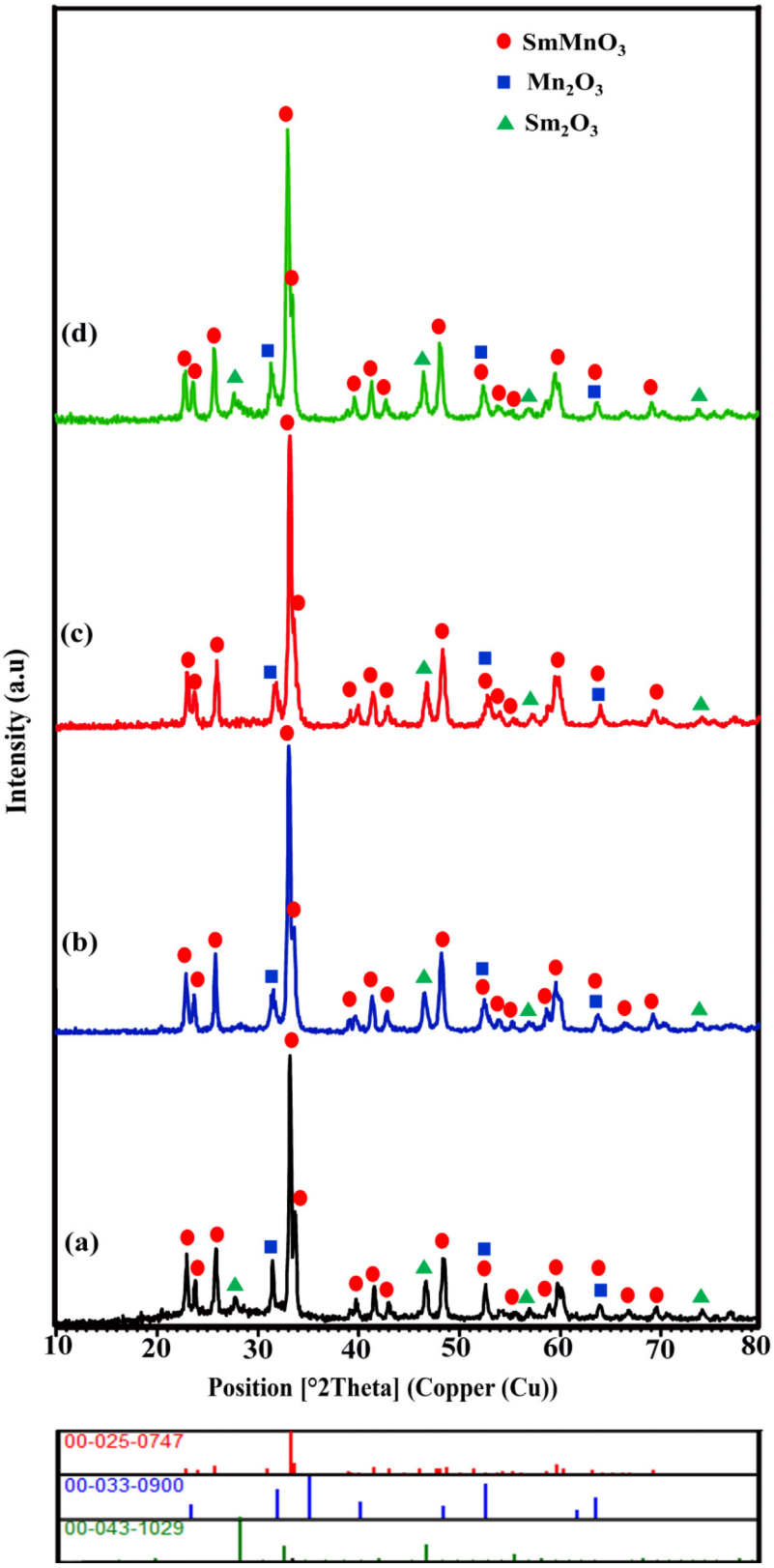

Fig. 1. XRD patterns of auto-combustion synthesized Sm-Mn-O nanostructures in the presence of different sugars (a-d) the samples 1–4.

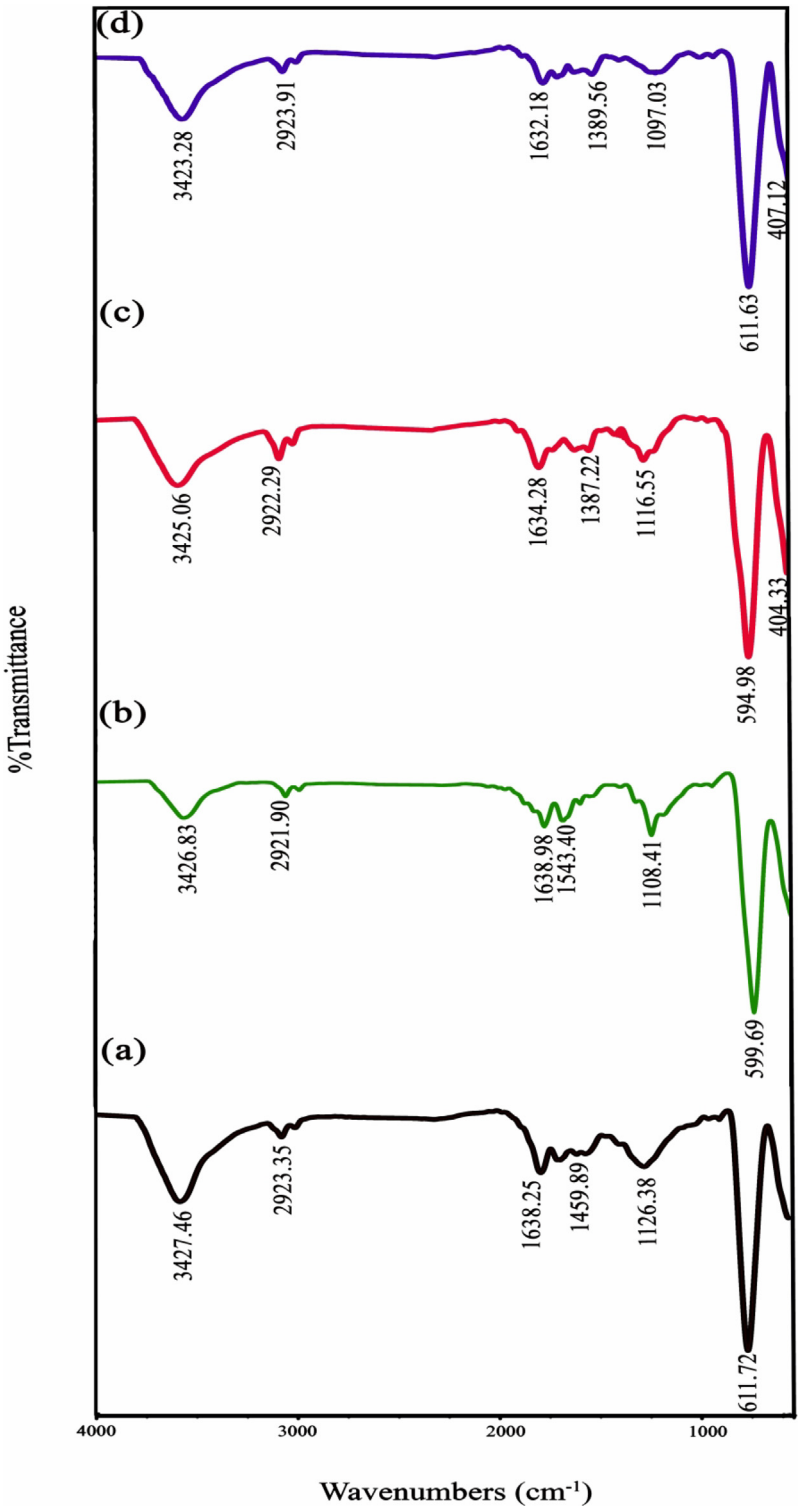

Fig. 2. FT-IR spectra of auto-combustion synthesized Sm-Mn-O nanostructures in the presence of different sugars (a-d) the samples 1–4.

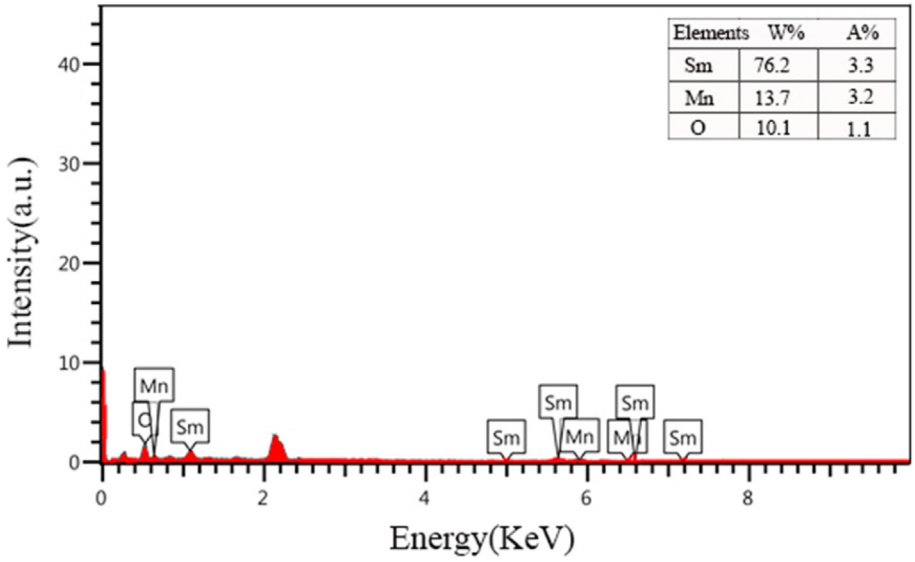

Fig. 3. EDS spectrum of the $SmMnO_3/Sm_2O_3/Mn_2O_3$ nanocomposites prepared by employing maltose as fuel and capping agent (sample 3).

Sm_2O_3/Mn_2O_3 nanocomposites were discussed by the photodegradation of organic dye pollutants in water under UV light.

2. Experimental

2.1. Materials

All the chemicals employed in this study were analytical grade and were applied without further purification. Samarium (III) nitrate hexahydrate ($Sm(NO_3)_3{\cdot}6H_2O$(, manganese (II) nitrate tetrahydrate ($Mn(NO_3).4H_2O$(, glucose ($C_6H_{12}O_6$), maltose ($C_{12}H_{22}O_{11}$), fructose ($C_6H_{12}O_6$) and starch ($(C_6H_{10}O_5)_n$) were purchased from Merck Company. Also, benzoic acid (BA), ethylenediaminetetraacetic acid (EDTA), and 1,4-benzoquinone (BQ) were purchased from Sigma-Aldrich and applied without further purification.

2.2. Synthesis of samarium manganite nanostructures

In this study, the nano-sized samarium manganite perovskites were fabricated through an eco-friendly sol–gel auto combustion route (Scheme 1). As a first step, 1 mmol of $Sm(NO_3)_3{\cdot}6H_2O$ and 1 mmol of $Mn(NO_3)_2{\cdot}4H_2O$ were separately dissolved in 15 ml of distilled water to form a homogeneous solution. After that, 3 mmol of saccharides as fuel was liquefied in 15 ml of distilled water and next the homogenized solution was dropwise added to $Sm(NO_3)_3{\cdot}6H_2O$ solution under magnetic stirring. Following 15 min of stirring and heating at 50 °C, the solution containing Mn $(NO_3)_2{\cdot}4H_2O$ was introduced drop-wise to the above solution. In this step, the temperature of the as-prepared mixture was raised to 120 °C for 90 min. Upon reaching the viscous solution, the reaction was completed. Lastly, the precipitate was dried in an oven at 70 °C and subsequently was calcined at 900 °C for 3 h. The presence of different saccharides as both fuel and capping agent was investigated for achieving the best product (Table 1).Table 2.

2.3. Physical instruments

An X-ray diffraction (XRD) analysis was carried out on a Philips-X'pertpro, X-ray diffractometer using Cu Kα monochromatized radiation (λ = 15.4 nm) to evaluate the crystal structure and phase purity of the fabricated perovskites. Field emission scanning electron microscopy (FE-SEM, Mira3 tescan) and transmission electron microscopy (TEM, JEM-2100) were employed for the evaluation of microscopic morphology of the samples. The element composition of auto-combustion synthesized Sm-Mn-O nanostructures was registered *via* employing a Philips XL30 microscope equipped with energy dispersive spectrometry (EDS) analysis at 20 kV stimulating charge. Diffuse reflectance UV–vis spectroscopy was performed with a Shimadzu UV/3101 PC ranging from 200 and 900 nm. The magnetic nature was collected by a vibrating sample magnetometer (VSM) (Desert Precision Magnetism Company, Kashan Kavir, and Iran). Also, the Brunauer–Emmett–Teller (BET) surface area of the optimized nano-photocatalyst was defined through N_2 adsorption (ADS)-desorption (DES) isotherms at −196 °C using an automatic gas adsorption analysis device (Tristar 3000, Micromeritics).

2.4. Photocatalytic tests

The Photocatalytic performance of as-prepared Sm-Mn-O nanostructures was evaluated by degradation of diverse contaminant models such as Rhodamine B (RhB), Erythrosine (EY), Methyl violet (MV) and Methyl orange (MO) at ambient conditions under UV light. The photocatalytic efficiencies of as-obtained nanopowders were explored in a closed cylindrical Pyrex reactor including the aqueous dye solution (30 ml, 10 ppm) and the catalyst (0.03 g). The suspension was aerated in the dark with constant magnetic stirring for 30 min to get adsorption – desorption equilibrium between catalyst and aqueous solution. During photoreaction, analytical suspension were sampled from each quartz tube and centrifuged to remove the nano-photocatalyst. UV light photocatalytic activity of as-obtained Sm-Mn-O nanocomposites was quantified *via* the concentration analysis of the remaining dye solution with a UV – vis spectrophotometer. The removal percentages (D%) of pollutant in aqueous solution can be calculated by the following steps:

$$D\% = (A_0 - A_t)/A_0 \times 100 \quad (1)$$

where A_0 and A_t are the absorption of aqueous solution at 0 and t minute, respectively.

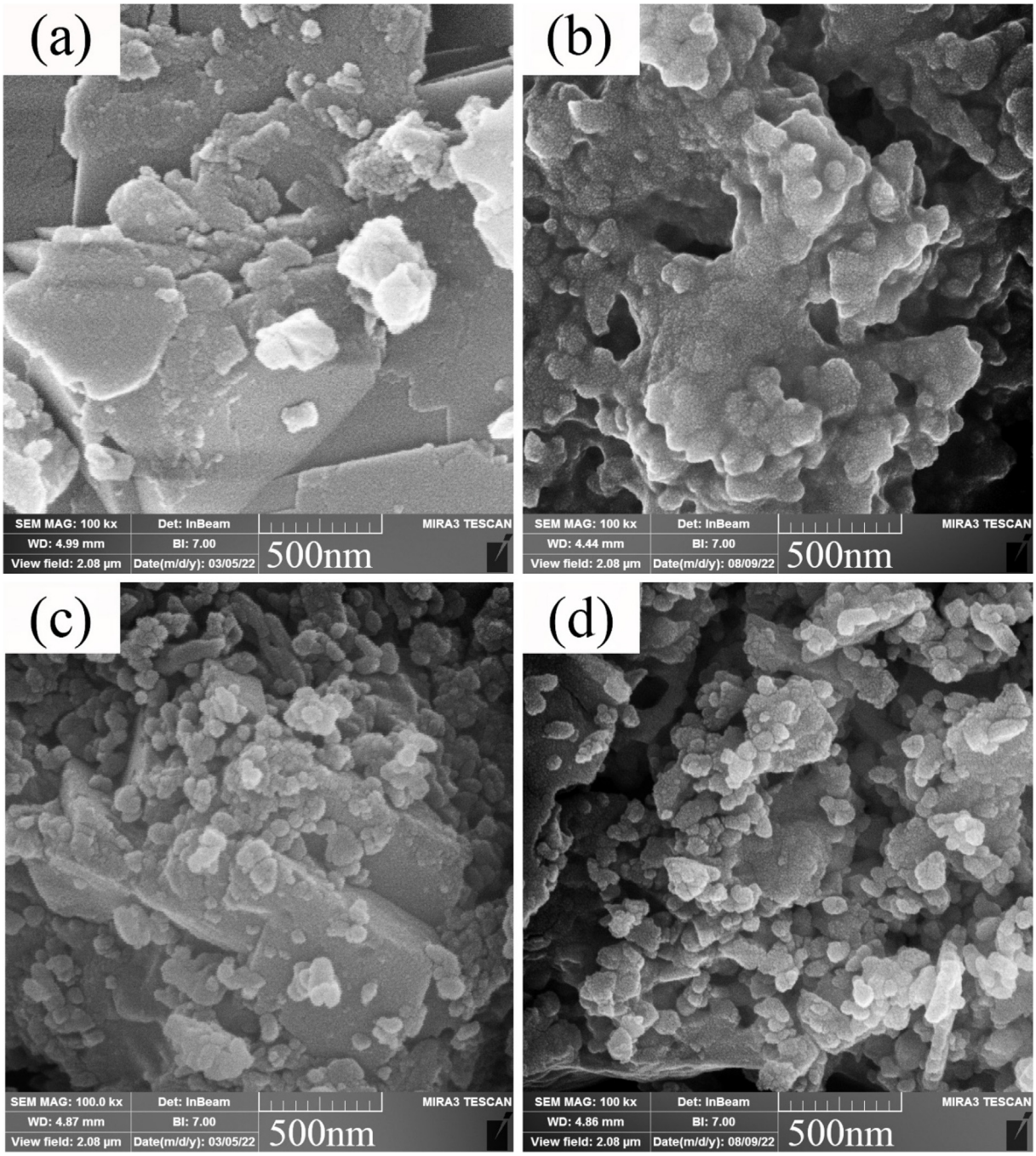

Fig. 4. FE-SEM micrographs of nano-sized samarium manganese perovskites (a-d) the samples 1–4.

3. Results and discussion

3.1. Crystallographic structure

To verify the effect of the different chemical saccharides including glucose, fructose, maltose and starch on the crystallographic structure of as-synthesized samples, XRD patterns were recorded in Fig. 1. As can be seen, diffraction lines are in acceptable conformity with perovskite-type $SmMnO_3$ structures with reference code 00-025-0747 as major phase (Liu et al., 2018). However, it is revealed that there are additional peaks with 2θ values of 27.7°, 46.6°, 57.0°, and 74.1° corresponding to the cubic phase of Sm_2O_3 with reference code 00-043-1029. Besides, all samples uncovers the reflections at 31.4°, 52.5°, and 63.9° as the well-documented rhombohedral phase of Mn_2O_3 with reference code 00-033-0900. Analysis of the XRD studies of samarium manganese perovskites synthesized in the presence of four different fuels confirms that the peak positions at the 2θ range of 10-80° are consistent with a mixture of three compounds, namely, $SmMnO_3$, Sm_2O_3, and Mn_2O_3. The mean crystallite sizes of the products were measured through the Scherrer's formula as follow (Teymourinia et al., 2017):Fig. 2.

$$D_c = K\lambda/\beta \mathrm{Cos}\theta \quad (2)$$

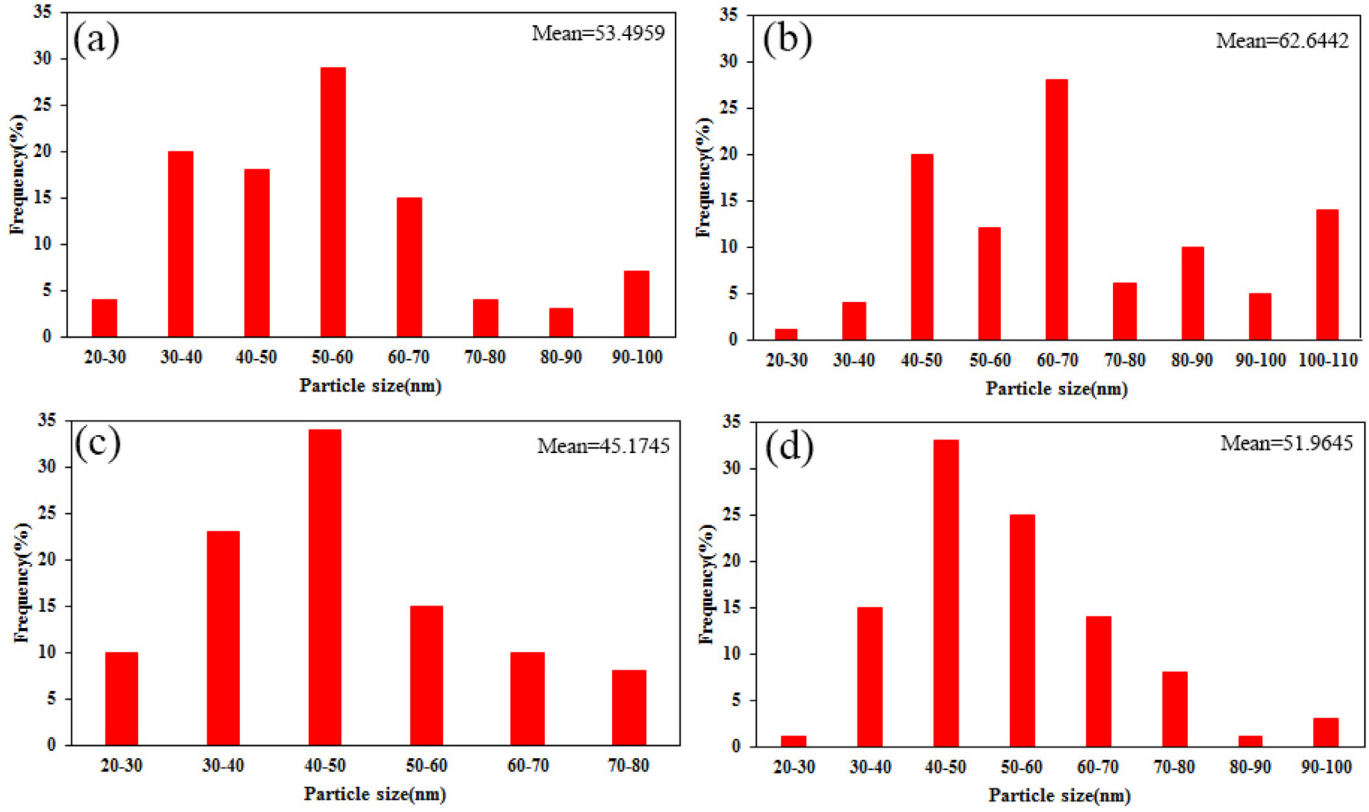

Fig. 5. Particle size distribution histograms of the samples (a) 1, (b) 2, (c) 3, and (d) 4.

where β is the width of the observed diffraction peak at its half maximum intensity (FWHM), K is the shape factor, which takes a value of about 0.9, and λ is the X-ray wavelength (CuKα radiation, equals to 0.154 nm). Table 1 list the crystallite sizes of the samples 1–4 ranging from 10.79 to 22.08 nm.

3.2. Bond structure

Fig. 2(a-d) illustrate the FT-IR spectra of the $SmMnO_3$-based ternary nanocomposites (samples 1–4) in the range of 400–4000 cm^{-1}. The absorption peaks at around ~ 3425 and 1634 cm^{-1} are associated with the O–H bond stretching and bending vibrations of adsorbed H_2O on the $SmMnO_3/Sm_2O_3/Mn_2O_3$ surface, respectively (Amiri et al., 2017; Panahi-Kalamuei et al., 2014). Furthermore, the peaks belonging to the asymmetric and symmetric C – H stretching modes of carbohydrate sugars are located at 2922 and 2855 cm^{-1}, respectively. The band observed at 1387 cm^{-1} can be assigned to the N–O bending vibration of nitrate ions (Li et al., 2009). FT-IR band at frequency of 1258 cm^{-1} is derived from the C-O-C stretching, which indicates the existence of sugar chains on the composite. There was a weak absorption peak at 1116 cm^{-1}, being characteristic for C–O–H stretching vibration of residual fuels (Sangsefidi et al., 2017). Also, the main characteristic bands in the window of 400–600 cm^{-1} are also related to the metal–oxygen (namely, Mn–O stretching, Sm–O stretching and O–Mn–O bending) modes (Hannora and Hanna, 2019; Lin et al., 2012).

Additionally, the chemical purity of rationally designed $SmMnO_3$-based ternary oxides was examined by EDS analysis. The supplied results in Fig. 3 reveals the coexistence of Sm, Mn and O elements in the as-obtained composite (sample 3).

3.3. Morphology studies

The influence of different saccharide sugars on the morphology and surface features of the resultant samples was explored *via* employing FE-SEM studies. Fig. 4(a-d) compares the shape and particle size of the samples prepared in the presence of monosaccharides (glucose and fructose), disaccharide (maltose) and polysaccharide (starch) in the 500 nm scale image. As described in the previous reports, development of low-cost auto-combustion process using carbohydrate sugars as a capping agent, fuel, and reductants is considered to be as an eco-friendly method, which possesses suitable physical and chemical modification (Köferstein et al., 2013; Sun et al., 2012). Following the introduction of glucose precursor (Fig. 4a), the composite structures suffer from overgrowth and particle agglomeration. With the addition of fructose, shown in Fig. 4b, the trend of growth of particles is quite clear and agglomeration is increased. These phenomena are caused by the inability of enough coverings of monosaccharaides having less carbonyl and hydroxyl groups on the growing crystal. However, the morphology of the $SmMnO_3/Sm_2O_3/Mn_2O_3$ nanocomposites fabricated in the presence of maltose unveils a reduction in particle diameter and a uniform growth (Fig. 4c). In conclusion, it is noticed that the inclusion of higher steric hindrance effect on crystal surfaces can limit the growth rate and results in an increase in uniformity. In Fig. 4d, the products exhibit the mass structures and interconnected particles when starch sugar with a long chain of hydroxyl groups was employed as fuel and capping agent. It is possible that an extreme situation between hydroxyl groups of starch supports the particles to grow larger. Histograms of particle size distributions have also been plotted for designed products and are shown in Fig. 5. Based on these results, we conclude that the ternary $SmMnO_3/Sm_2O_3/Mn_2O_3$ nanocomposites prepared with

maltose exhibit the best uniformity and the smallest average particle size. Furthermore, to verify the shape and morphology of selected nanoparticles, the composite geometries of the sample 3 was determined by TEM analysis. The TEM micrographs portrayed in Fig. 6 confirms that the particles were uniformly arranged in a cubical manner within a homogenous structure. The particles exhibit a size distribution ranging from 25 to 35 nm.

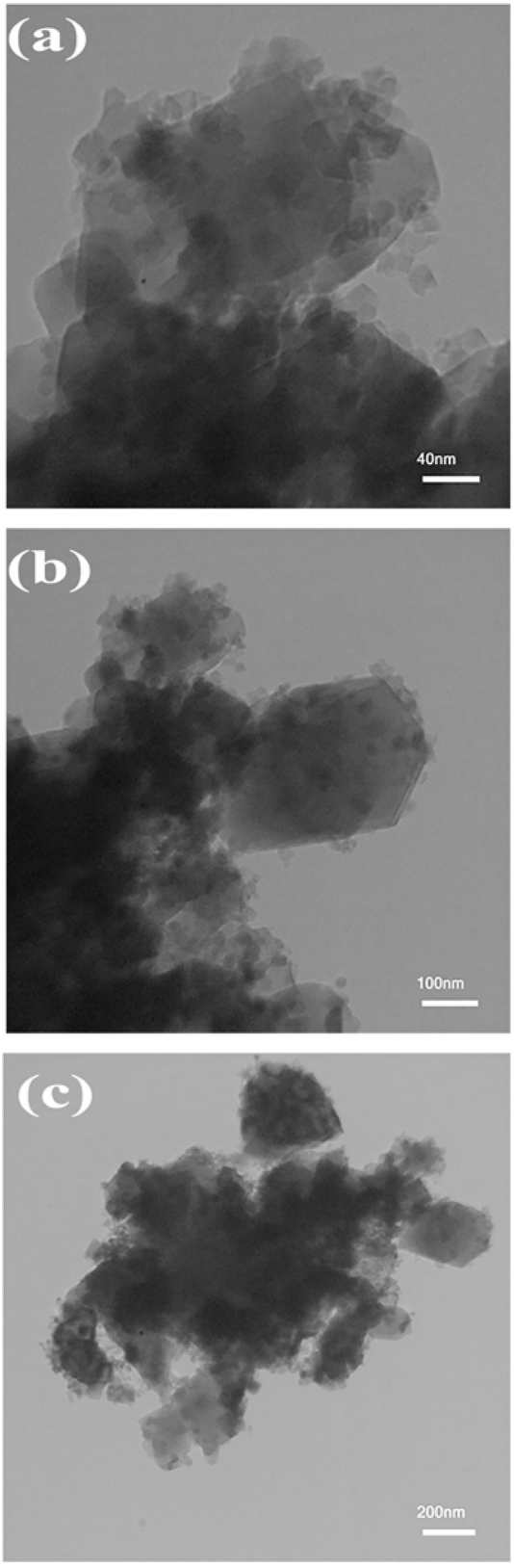

Fig. 6. TEM images of the $SmMnO_3/Sm_2O_3/Mn_2O_3$ nanocomposites prepared with maltose (sample 3) at different magnifications.

3.4. VSM analysis

The magnetic property of optimized $SmMnO_3/Sm_2O_3/Mn_2O_3$ nanocomposites (sample 3) was studied using a vibrating sample magnetometer (VSM) at room temperature. As illustrated in Fig. 7, ternary oxide compound follow a typical paramagnetic behavior with a maximum saturation magnetization (Ms) of 0.359 emu/g.

3.5. BET analysis

Based on the BET technique, a survey for detecting the N_2 ADS-DES isotherms at 77 k, the textural and surface characteristics of the $SmMnO_3/Sm_2O_3/Mn_2O_3$ nanocomposites was measured. Fig. 8 (a, b) plots the ADS-DES isotherm and BJH curve of the sample 3. By involving the International Union of Pure and Applied Chemistry (IUPAC) category, this composite was introduced as a type III isotherm. In Fig. 8b, the pore size distribution of ternary oxides has been supplied. The pore volume and pore diameter of the $SmMnO_3/Sm_2O_3/Mn_2O_3$ nanocomposites were calculated as 0.0088713 cm^3/g and 1.66 nm, respectively.

3.6. Optical properties

Fig. 9 records the intensive absorption and the light harvesting ability of as-prepared nanocomposites (samples 1–4) through DRS measurement. In DRS profiles, the optical bandgap (B.G.) is concluded *via* the plot of $(\alpha h\upsilon)^2$ *vs.* $h\upsilon$ by employing the Tauc relation (Tauc, 1968), which is expressed as:

$$(\alpha h\upsilon)^n = A(h\upsilon - B.G.) \quad (3)$$

where υ is the light frequency. h shows Planck constant (6.626×10^{-34} J s). α, A and B.G. represents the absorbance, material constant, and optical bandgap, respectively. From linear extrapolation of $(\alpha h\upsilon)^2$ versus $h\upsilon$ to zero (inset of Fig. 9(a-d)), the $SmMnO_3/Sm_2O_3/Mn_2O_3$ nanocomposites illustrate two distinct absorption edge in the UV region for samples 1–4. The estimated band gap values of these samples are centered at about 3.2–3.4 eV for $SmMnO_3$ and Mn_2O_3 components as well as 3.6–3.9 eV for Sm_2O_3 (Duc Dung et al., 2013; Putri et al., 2020).

3.7. Photocatalytic activity

The photodegradation behavior of the $SmMnO_3/Sm_2O_3/Mn_2O_3$ nanocomposites over the decoloration of two various groups of organic pollutant such as cationic (MV, RhB) and anionic (EY, MO) dyes were comprehensively investigated under UV light irradiation. In Fig. 10, a comparative analysis of the impression of diverse dyes species over three distinct catalysts (samples 1, 3 and 4) was accomplished to achieve better performance. As noticed in Fig. 10a, the removal efficiency yield of MV in the presence of the samples 1, 3 and 4 was about 27.48%, 46.68%, and 43.59%, respectively. Under similar conditions, RhB degradation on these catalysts in Fig. 10b exhibited approximately 36.56%, 26.11, and 28.63% of the efficiency after 120 min, respectively. By analyzing EY as organic pollutant (Fig. 10c), the degradation percentages were 35.39%, 30.98%, and 26.97% for sample 1, 3, and 4, respectively. However, when MO molecules were employed as model, the photocatalytic yield in Fig. 10d could removal 56.81%, 72.24%, and 64.13% after 120 min for sample 1, 3, and 4, respectively. As

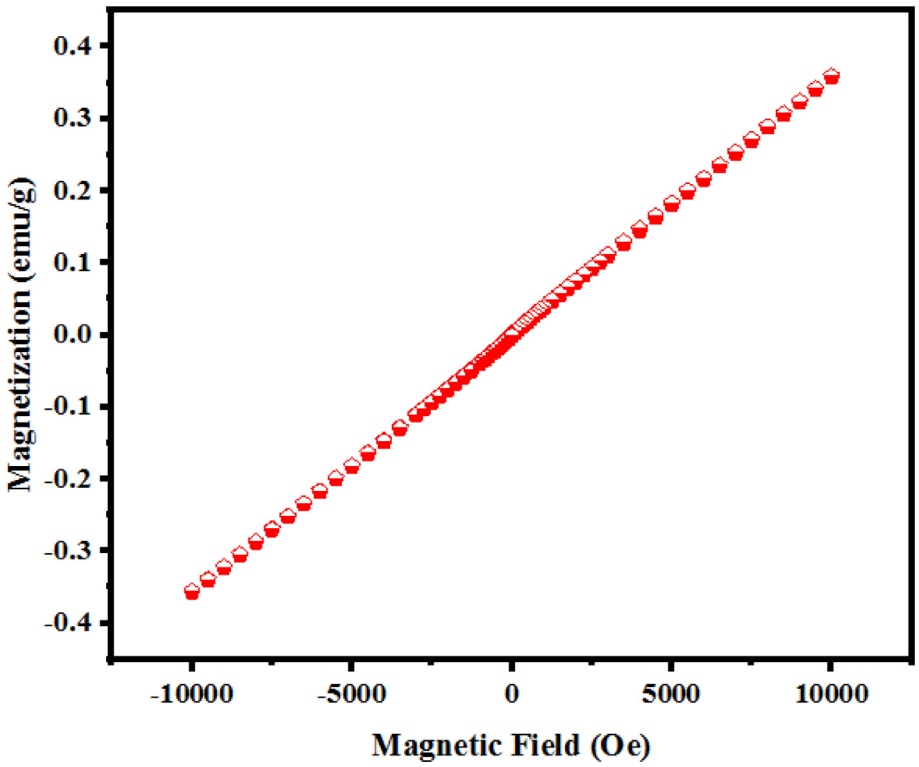

Fig. 7. VSM plot of the $SmMnO_3/Sm_2O_3/Mn_2O_3$ nanocomposites prepared with maltose (sample 3).

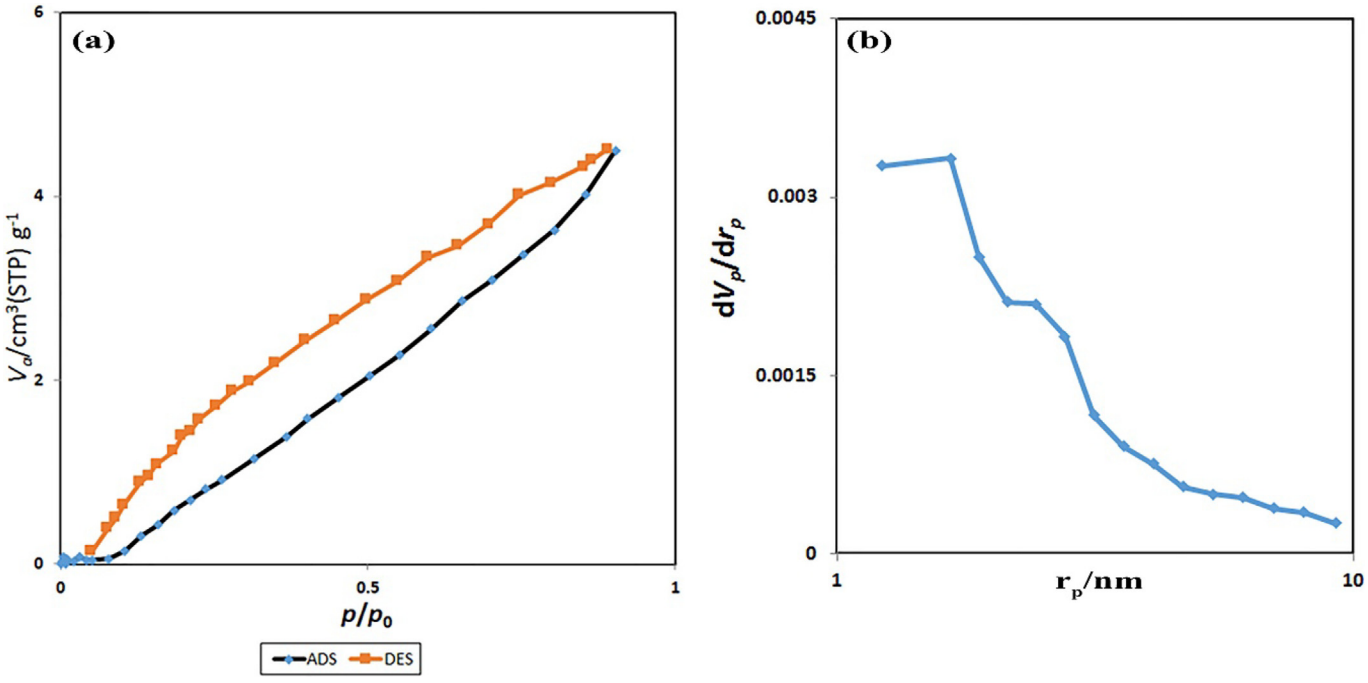

Fig. 8. (a) N_2 adsorption/desorption isotherm and (b) BJH pore size distribution of the $SmMnO_3/Sm_2O_3/Mn_2O_3$ nanocomposites (sample 3).

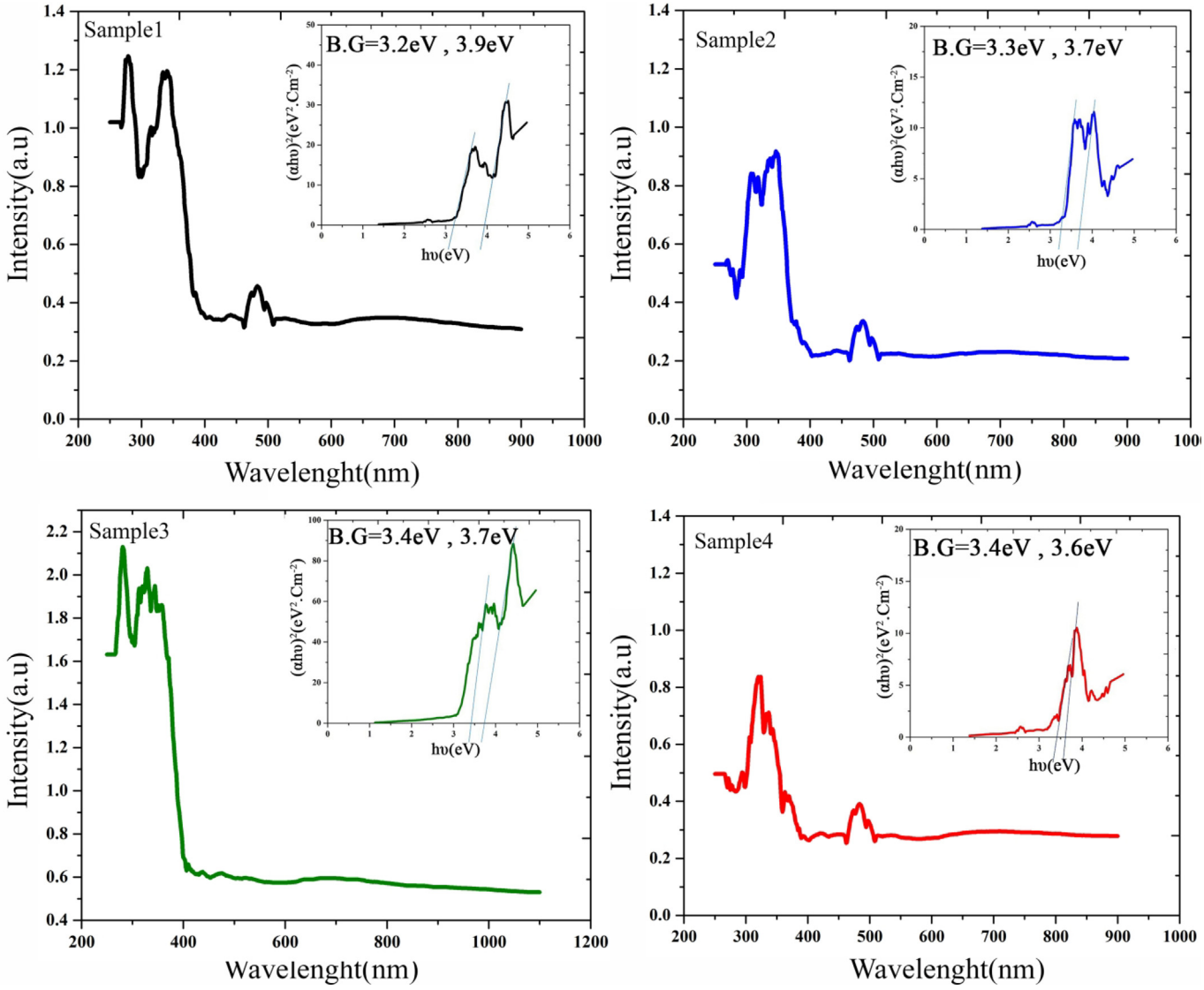

Fig. 9. UV–vis spectra and plots of $(\alpha h\nu)^2$ versus $(h\nu)$ of the $SmMnO_3/Sm_2O_3/Mn_2O_3$ nanostructures (a-d) the samples 1–4.

a result of these tests, it can be seen that the $SmMnO_3/Sm_2O_3/Mn_2O_3$ nanocomposites synthesized in the presence of maltose as both fuel and capping agent provide best response for the destruction of MO molecules. Therefore, for verifying how MO concentration affects the catalyst's efficiency, an example of the photocatalytic experiments on the concentration of the contaminant was further studied. Fig. 10e depicts the influences of a variety of MO concentrations (5, 10, and 15 ppm) in the photocatalytic process of the $SmMnO_3/Sm_2O_3/Mn_2O_3$ nanocomposites (sample 3) under UV light illumination for 120 min. The photoreaction efficiency of the resulting nanocomposites was confirmed to increase up to the MO concentration of 10 ppm and exhibited to decrease on further increase in dye concentration (15 ppm). In this context, 48.08% and 65.65% dye removal percentages were obtained with the pollutant concentrations of 5 and 15 ppm, respectively. A decrease in efficiency of 15 ppm concentration of MO can probably related to the competition for the available binding sites on the photocatalyst surface. Since the reaction mechanism in typical heterogeneous photocatalytic processes can pose an additional degree of enhanced light harvesting ability account, we followed the Langmuir-Hinshelwood (L-H) model to understand the possible reaction kinetics of the photocatalytic reactions at different conditions as (Zinatloo-Ajabshir et al., 2021):

$$\ln(C_0/C) = kt \quad (4)$$

where C_0, C and k are the primary dye concentration, concentration at t time, and the degradation rate constant of the pseudo-first-order reaction (min^{-1}), respectively. According to the linear logarithmic plots in Fig. 11(a-e), it can be concluded that the best degradation constant value of 0.0101 min^{-1} is present for the sample 3 at 10 ppm of MO molecules, validating maximum photocatalytic efficiency.

Subsequent, to gain underlying mechanism of the active species involved in the photoreaction of MO over the $SmMnO_3/Sm_2O_3/Mn_2O_3$ nanocomposites, the trapping nature of BA, EDTA, and BQ were directly discriminated as scavengers for $^{\bullet}OH$, h^+, and $^{\bullet}O_2^-$, respectively (Panahi et al., 2023). Analysis of Fig. 12(a-c) illustrates that introduction of BA has a minor effect on charge of the degradation of MO for three distinct samples (1, 3 and 4). However, with addition of EDTA, and BQ into the reaction solution, degradation efficiency was significantly decreased, indicating that h^+, and $^{\bullet}O_2^-$ possess a major impact on the photodegradation of MO. The pro-

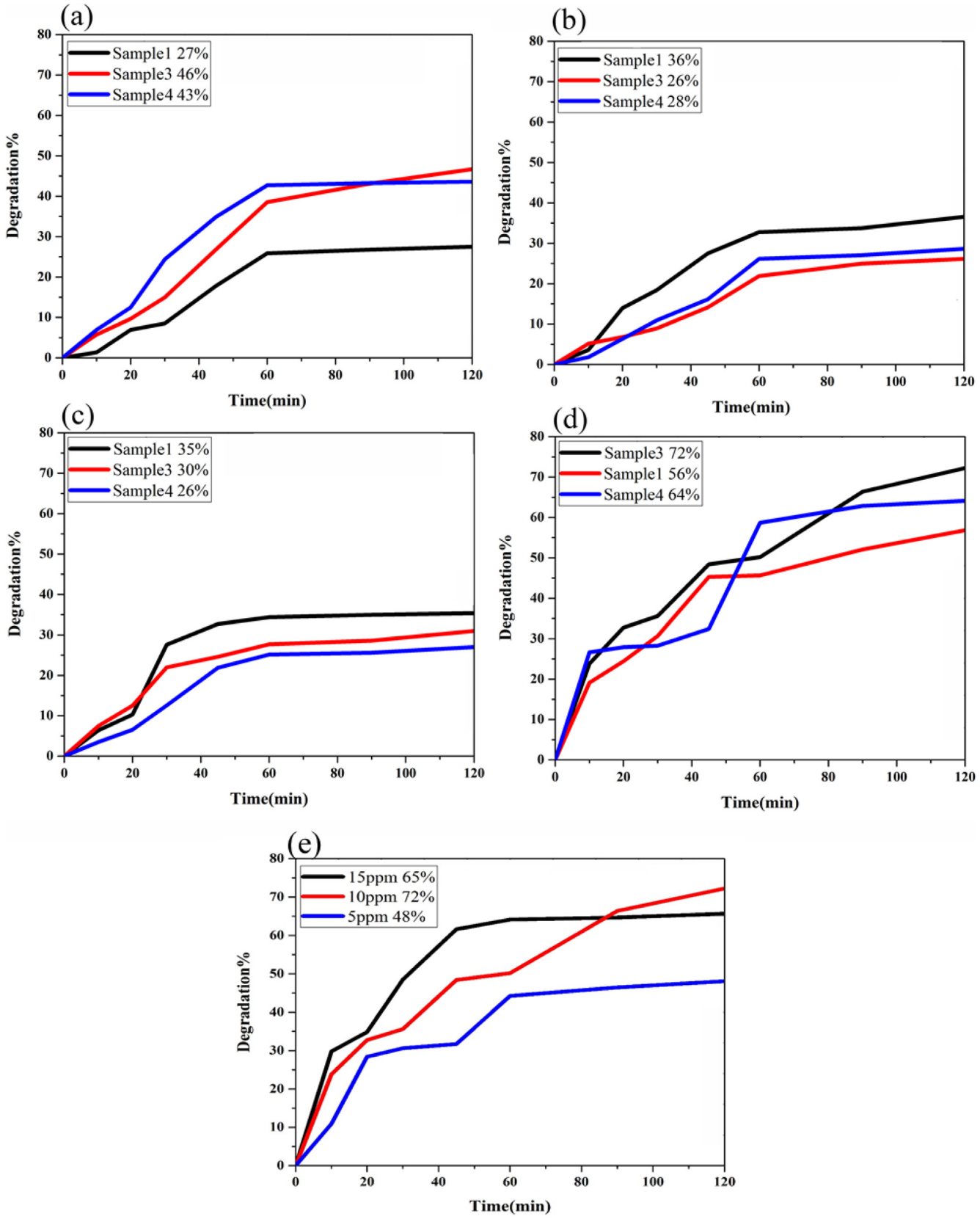

Fig. 10. The photocatalytic efficiencies for the degradation of four different dyes with 10 ppm concentration; (a) MV, (b) RhB, (c) EY, (d) MO over the Sm-Mn-O nanostructures (samples 1, 3, and 4) and (e) effect of different concentrations of MO over the sample 3 under UV light irradiation.

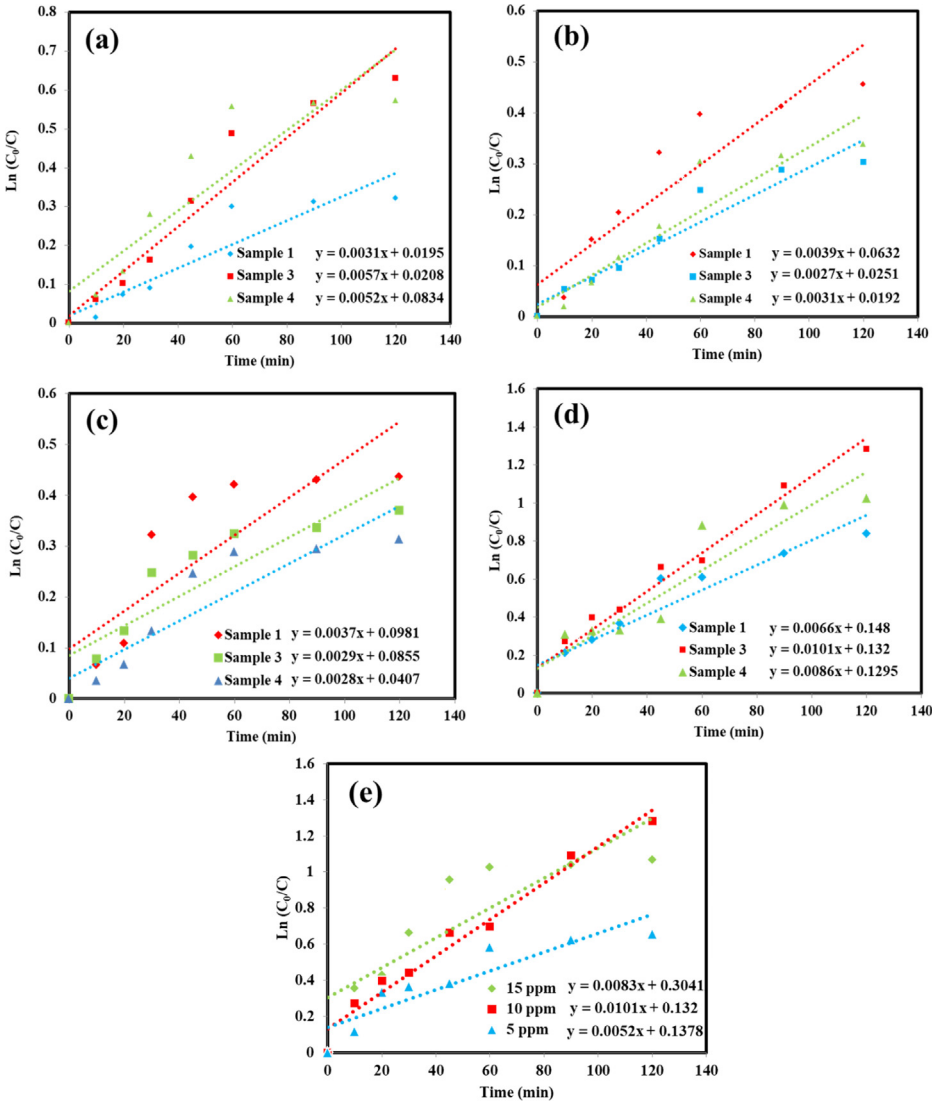

Fig. 11. Plots of $\ln(C_0/C)$ *vs* time for four different dyes with 10 ppm concentration; (a) MV, (b) RhB, (c) EY, (d) MO in the presence of the $SmMnO_3/Sm_2O_3/Mn_2O_3$ nanocomposites synthesized by diverse sugars (samples 1, 3, and 4) and (e) effect of different concentrations of MO over the sample 3 under UV light irradiation.

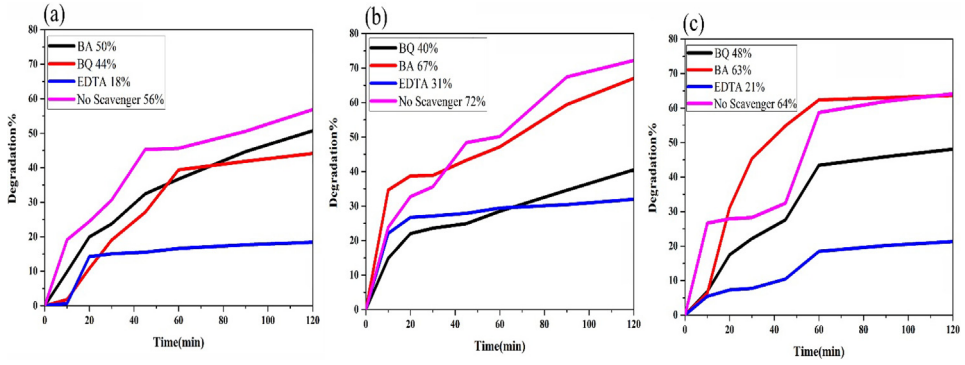

Fig. 12. Effect of various scavengers over the samples (a) 1, (b) 3 and (c) 4 in the photocatalytic degradation of 10 ppm MO under UV light.

posed operative mechanism to the decolorization of MO under UV light is as (Konstantinou and Albanis, 2004):

$$SmMnO_3/Sm_2O_3/Mn_2O_3 + h\nu(UV) \rightarrow SmMnO_3/Sm_2O_3/Mn_2O_3\ (e_{CB}^- + h_{VB}^+) \quad (5)$$

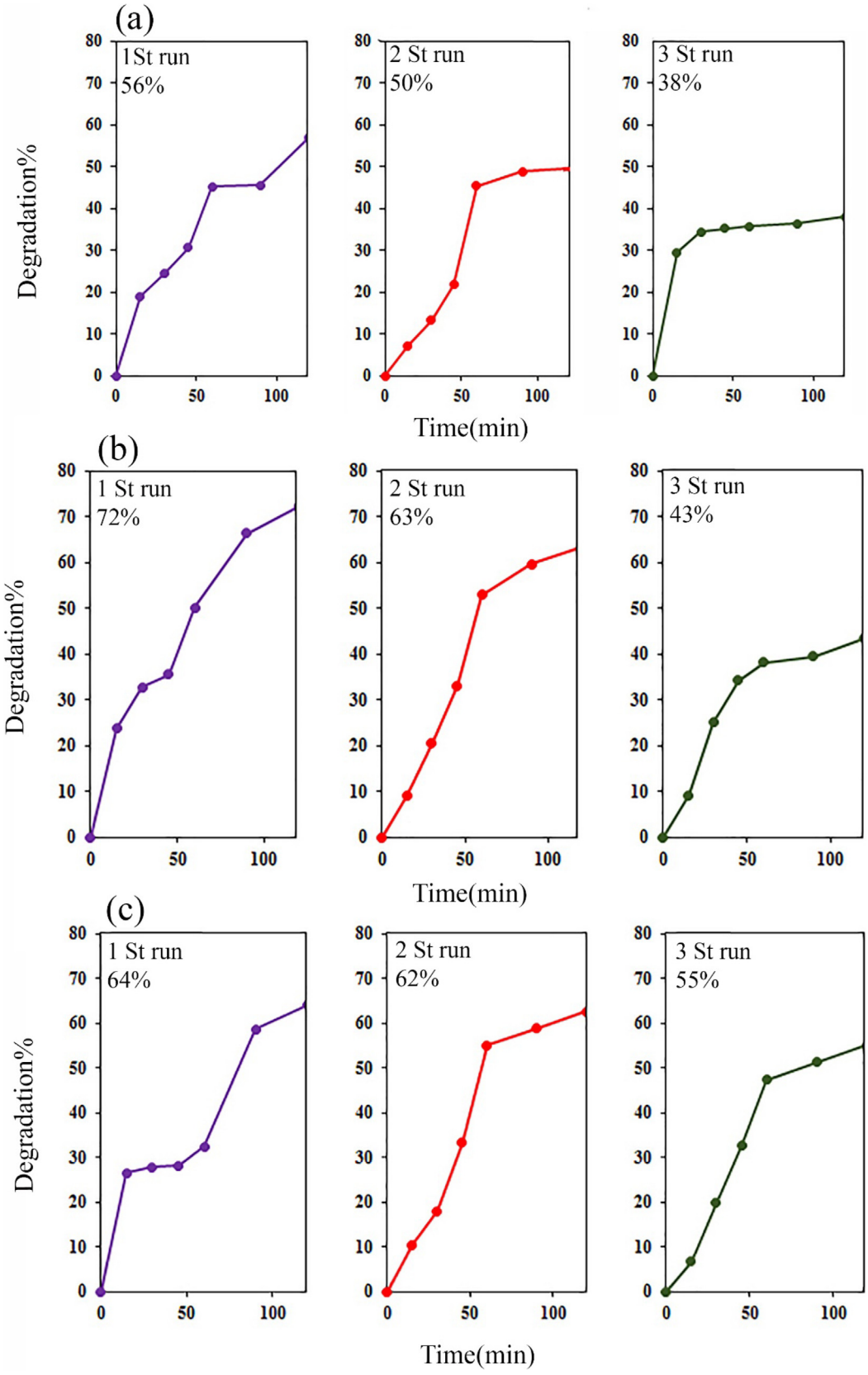

Fig. 13. Degradation efficiency of the samples (a) 1, (b) 3 and (c) 4 with increasing number of photocatalytic cycles.

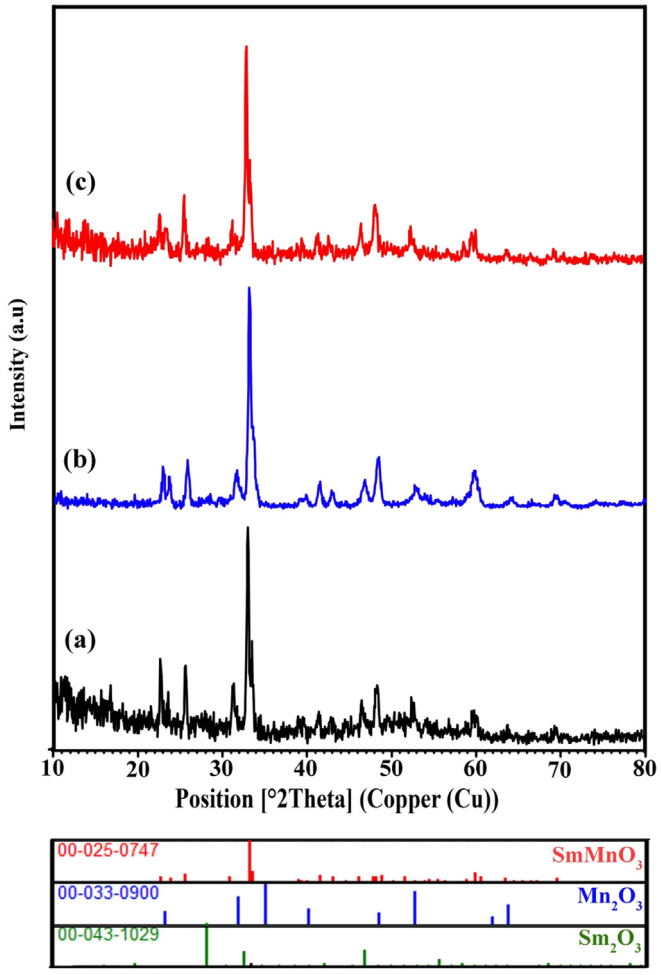

Fig. 14. XRD patterns of the samples (a) 1, (b) 3 and (c) 4 after photocatalytic runs.

$$SmMnO_3/Sm_2O_3/Mn_2O_3\ (h_{VB}^{+}) + H_2O \rightarrow SmMnO_3/Sm_2O_3/Mn_2O_3 + H^{+} + OH\bullet \quad (6)$$

$$SmMnO_3/Sm_2O_3/Mn_2O_3\ (e_{CB}^{-}) + O_2 \rightarrow SmMnO_3/Sm_2O_3/Mn_2O_3 + O_2\bullet^{-} \quad (7)$$

$$2H^{+} + \bullet O_2^{-} \rightarrow H_2O_2 \quad (8)$$

$$H_2O_2 + e^{-} \rightarrow OH^{-} + \bullet OH \quad (9)$$

$$h^{+} + OH^{-} \rightarrow \bullet OH \quad (10)$$

$$h^{+} + H_2O \rightarrow H^{+} + \bullet OH \quad (11)$$

$$e^{-} + O_2 \rightarrow \bullet O_2^{-} \quad (12)$$

$$O_2\bullet^{-} + H^{+} \rightarrow HO_2\bullet \quad (13)$$

$$\bullet O_2^{-} + H^{+} + e^{-} \rightarrow HOO\bullet \quad (14)$$

$$HOO\bullet + H_2O \rightarrow \bullet OH + H_2O_2 \quad (15)$$

$$h_{VB}^{+} + MO \rightarrow \text{oxidation products} \quad (16)$$

$$\bullet OH + MO \rightarrow \text{degradation products (e.g., } CO_2, H_2O, H_2) \quad (17)$$

$$e_{CB}^{-} + MO \rightarrow \text{reduction products} \quad (18)$$

Since the catalysts lifetime is of supreme importance parameters for the photocatalyst process in practical applications, the structural photostability and recyclability of the $SmMnO_3/Sm_2O_3/Mn_2O_3$ nanocomposites was explored after three consecutive cycles. As indicated in Fig. 13 (a-c), after three cycles, the degradation rate of the products synthesized in the presence of glucose (sample 1), maltose (sample 3) and starch (sample 4) still retains at a relatively high level. However, there is a some reduction in the performance due to the loss of photocatalyst powders during recycling. The photocatalytic activity of samples 1, 3, and 4 dropped form 56.81% to 38.89%, 72.24% to 43.42%, and 64.13% to 55.08%, respectively. To evaluate the crystallographic structure of reused samples, XRD results were analyzed (Fig. 14). The result suggests that the XRD patterns of fabricated nanocomposites keep unchanged following the three successive cycles of photocatalysis, describing high photostability of the $SmMnO_3/Sm_2O_3/Mn_2O_3$ nanocomposites.

4. Conclusions

In summary, with the help of environmentally friendly capping agents, novel $SmMnO_3/Sm_2O_3/Mn_2O_3$ nanocomposites were fabricated through combustion method for the decolorization of different water-soluble organic contaminants. Based on DRS results, as-formed compounds showed a suitable ability under UV light. Among the tested samples, the products prepared by maltose as fuel manifested the highest potential in removing 10 ppm MO after 120 min of UV irradiation. Under this circumstance, the superior rate constant ($k = 0.0101\ min^{-1}$) belongs to the maximum photocatalytic efficiency (72.24%). Further scavenger investigation confirmed that h^{+}, and $^{\bullet}O_2^{-}$ could be the most active radicals in the photocatalytic process. Also, the recycle experiments presented high stability of ternary $SmMnO_3/Sm_2O_3/Mn_2O_3$ nanocomposites with a relative loss in efficiency after three cycles.

CRediT authorship contribution statement

Mina Jamdar: Software, Investigation, Methodology, Formal analysis. **Zahra Heydariyan:** Formal analysis, Data curation, Investigation, Software. **Asaad H. Alzaidy:** Writing – review & editing, Resources, Visualization. **Elmuez A. Dawi:** Writing – review & editing, Resources, Visualization. **Masoud Salavati-Niasari:** Software, Formal analysis, Methodology, Writing – review & editing, Writing – original draft, Conceptualization, Methodology, Supervision, Project administration, Investigation, Data curation, Validation, Resources, Visualization, Funding acquisition.

Declaration of competing interest

The authors declare that they have no known competing financial interests or personal relationships that could have appeared to influence the work reported in this paper.

Acknowledgment

Authors are grateful to the council of Iran National Science Foundation (INSF, 97017837), and the University of Kashan for supporting this work by Grant No (159271/MJ1).

References

Amiri, M., Salavati-Niasari, M., Akbari, A., Gholami, T., 2017. Removal of malachite green (a toxic dye) from water by cobalt ferrite silica magnetic nanocomposite:

herbal and green sol-gel autocombustion synthesis. Int. J. Hydrogen Energy 42 (39), 24846–24860.
Duc Dung, D., Van Thiet, D., Anh Tuan, D., Cho, S., 2013. Strain effects in epitaxial Mn2O3 thin film grown on MgO (100). J. Appl. Phys. 113 (17).
Gadani, K., Keshvani, M., Dhruv, D., Boricha, H., Rathod, K., Prajapati, P., Joshi, A., Pandya, D., Shah, N., Solanki, P., 2017. Low field magnetoelectric and magnetotransport properties of sol–gel grown nanostructured LaMnO3 manganites. J. Alloys Compd. 719, 47–57.
Hannora, A.E., Hanna, F., 2019. Preparation of nanostructured manganites SmMnO 3 and Sm 0.5 Sr 0.5 MnO 3 by mechanochemical synthesis method. J. Mater. Sci.: Mater. Electron. 30, 12456–12464.
Honarmand, M., Golmohammadi, M., Naeimi, A., 2020. Green synthesis of SnO2-bentonite nanocomposites for the efficient photodegradation of methylene blue and eriochrome black-T. Mater. Chem. Phys. 241, 122416.
Ji, R., Liu, J., Zhang, T., Peng, Y., Li, Y., Chen, D., Xu, Q., Lu, J., 2021. Construction of a ternary Z-scheme In2S3@ Au@ P3HT photocatalyst for the degradation of phenolic pollutants under visible light. Sep. Purif. Technol. 272, 118787.
Köferstein, R., Walther, T., Hesse, D., Ebbinghaus, S.G., 2013. Preparation and characterization of nanosized magnesium ferrite powders by a starch-gel process and corresponding ceramics. J. Mater. Sci. 48, 6509–6518.
Konstantinou, I.K., Albanis, T.A., 2004. TiO2-assisted photocatalytic degradation of azo dyes in aqueous solution: kinetic and mechanistic investigations: a review. Appl. Catal. B: Environ. 49 (1), 1–14.
Kumar, R.D., Thangappan, R., Jayavel, R., 2017. Study on the effect of annealing temperature and photocatalytic properties of TbMnO3 nanoparticles. Optik 138, 365–371.
Kumar, R.D., Thangappan, R., Jayavel, R., 2019. Structural, morphological and photocatalytic activity of YMnO3 nanorods. J. Nanosci. Nanotechnol. 19 (4), 2385–2390.
Li, Y., Yao, S., Xue, L., Yan, Y., 2009. Sol–gel combustion synthesis of nanocrystalline LaMnO 3 powders and photocatalytic properties. J. Mater. Sci. 44, 4455–4459.
Lin, G., Yang, H., Xian, T., Wei, Z., Jiang, J., Feng, W., 2012. Synthesis of TbMnO3 nanoparticles via a polyacrylamide gel route. Adv. Powder Technol. 23 (1), 35–39.
Liu, L., Jia, J., Sun, T., Zhang, H., 2018. A facile method for scalable preparation of mesoporous structured SmMnO3 perovskites sheets for efficient catalytic oxidation of toluene. Mater. Lett. 212, 107–110.
Luo, J., Chen, J., Guo, R., Qiu, Y., Li, W., Zhou, X., Ning, X., Zhan, L., 2019. Rational construction of direct Z-scheme LaMnO3/g-C3N4 hybrid for improved visible-light photocatalytic tetracycline degradation. Sep. Purif. Technol. 211, 882–894.
Mehdizadeh, P., Orooji, Y., Amiri, O., Salavati-Niasari, M., Moayedi, H., 2020. Green synthesis using cherry and orange juice and characterization of TbFeO3 ceramic nanostructures and their application as photocatalysts under UV light for removal of organic dyes in water. J. Clean. Prod. 252, 119765.
Michel, C.R., Lopez-Alvarez, M.A., Martínez-Preciado, A.H., Carbajal-Arízaga, G.G., 2019. Novel UV sensing and photocatalytic properties of DyCoO3. J. Sens. 2019, 1–12.
Panahi, A., Monsef, R., Dawi, E.A., Hussein, A.S., Salavati-Niasari, M., 2023. Green auto-combustion synthesis and characterization of TmVO4 nanostructures in the presence carbohydrate sugars and their application as Visible-light photocatalyst. Sol. Energy 258, 372–382.
Panahi-Kalamuei, M., Salavati-Niasari, M., Hosseinpour-Mashkani, S.M., 2014. Facile microwave synthesis, characterization, and solar cell application of selenium nanoparticles. J. Alloys Compd. 617, 627–632.
Paul, S., Anand, V., Duggal, V., 2023. Preparation and performance of a Sr2+ doped LaMnO3 cathode for low temperature solid oxide fuel cells. Mater. Today: Proc.
Piao, C., Chen, L., Liu, Z., Tang, J., Liu, Y., Lin, Y., Fang, D., Wang, J., 2021. Construction of solar light-driven dual Z-scheme Bi2MoO6/Bi2WO6\AgI\Ag photocatalyst for enhanced simultaneous degradation and conversion of nitrogenous organic pollutants. Sep. Purif. Technol. 274, 119140.
Putri, N., Yulizar, Y., Umar, A., Apriandanu, D., 2020. Sm2O3 nanoparticles preparation using caesalpinia pulcherrima leaf extract, characterization and photocatalytic activity, IOP Conference Series: Mater. Sci. Eng. IOP Publishing, p. 012012.
Romaguera-Barcelay, Y., Matos, R.S., Pedraça, A.S., de Cruz, J.P., Brito, W.R., Oliveira, R.M., Henrique Filho, D., 2021. Advanced spatial investigation of 3D nanoscale topography of DyMnO3 thin films. Phys. B: Condens. Matter 623, 413360.
Sadegh, F., Politakos, N., de San Román, E.G., Sanz, O., Perez-Miqueo, I., Moya, S.E., Tomovska, R., 2020. A green synthesis of nanocatalysts based on reduced graphene oxide/magnetic nanoparticles for the degradation of Acid Red 1. RSC Adv. 10 (64), 38805–38817.
Sajadi, S.M., Pirouei, M., Salih, N.A., Kolo, K., Hamad, S.M., 2020. Rapid ecosynthesis of TiO 2@ CuO@ Chromite nanocatalyst for environmentally friendly applications: solventless cyanation of aldehydes and high efficient treatment of sewage waters. Environ. Sci. Eur. 32, 1–15.
Sangsefidi, F.S., Nejati, M., Verdi, J., Salavati-Niasari, M., 2017. Green synthesis and characterization of cerium oxide nanostructures in the presence carbohydrate sugars as a capping agent and investigation of their cytotoxicity on the mesenchymal stem cell. J. Clean. Prod. 156, 741–749.
Sun, J., Wang, Z., Wang, Y., Zhu, Y., Shen, T., Pang, L., Wei, K., Li, F., 2012. Synthesis of the nanocrystalline CoFe2O4 ferrite thin films by a novel sol–gel method using glucose as an additional agent. Mater. Sci. Eng. B 177 (2), 269–273.
Tauc, J., 1968. Mater. Res. Bull. 3, 37–46.
Teymourinia, H., Salavati-Niasari, M., Amiri, O., Safardoust-Hojaghan, H., 2017. Synthesis of graphene quantum dots from corn powder and their application in reduce charge recombination and increase free charge carriers. J. Mol. Liq. 242, 447–455.
Verma, M., Ahmad, W., Park, J.-H., Kumar, V., Vlaskin, M.S., Vaya, D., Kim, H., 2022. One-step functionalization of chitosan using EDTA: Kinetics and isotherms modeling for multiple heavy metals adsorption and their mechanism. J. Water Process Eng. 49, 102989.
Verma, N., Chundawat, T.S., Chandra, H., Vaya, D., 2023. An efficient time reductive photocatalytic degradation of carcinogenic dyes by TiO2-GO nanocomposite. Mater. Res. Bull. 158, 112043.
Wahba, M.A., Sharmoukh, W., Yakout, S.M., Khalil, M.S., 2022. Fast and full spectrum sunlight photocatalysts: Fe/Co or Ni implanted multiferroic LaMnO3. Opt. Mater. 124, 111973.
Wu, Y., Du, X., Kou, Y., Wang, Y., Teng, F., 2019. Mesoporous SiO2 nanostructure: light-induced adsorption enhancement and its application in photocatalytic degradation of organic dye. Ceram. Int. 45 (18), 24594–24600.
Xing, S., Song, S., Xiang, J., 2021. Structural, Optical, Magnetic, and Photocatalytic Properties of Multiferroic RMnO 3 (R= Tb, Dy, Ho) Nanoparticles Obtained through Microwave Assisted Acrylamide Gel Route. Russ. J. Phys. Chem. A 95, 1033–1042.
Yadav, R., Chundawat, T.S., Surolia, P.K., Vaya, D., 2022. Photocatalytic degradation of ortho-nitrophenol using ZnO-β-CD nanocomposite. ChemistrySelect 7 (23), e202200394.
Yue, B., Hu, Q., Ji, L., Wang, Y., Liu, J., 2019. Facile synthesis of perovskite CeMnO 3 nanofibers as an anode material for high performance lithium-ion batteries. RSC Adv. 9 (65), 38271–38279.
Zhang, G., Chen, D., Li, N., Xu, Q., Li, H., He, J., Lu, J., 2019a. Fabrication of Bi2MoO6/ZnO hierarchical heterostructures with enhanced visible-light photocatalytic activity. Appl. Catal. B: Environ. 250, 313–324.
Zhang, Y., Ma, C., Yang, X., Song, Y., Liang, X., Zhao, X., Wang, Y., Gao, Y., Liu, F., Liu, F., 2019b. NASICON-based gas sensor utilizing MMnO3 (M: Gd, Sm, La) sensing electrode for triethylamine detection. Sens. Actuators B: Chem. 295, 56–64.
Zinatloo-Ajabshir, S., Mousavi-Kamazani, M., 2021. Recent advances in nanostructured Sn− Ln mixed-metal oxides as sunlight-activated nanophotocatalyst for high-efficient removal of environmental pollutants. Ceram. Int. 47 (17), 23702–23724.
Zinatloo-Ajabshir, S., Baladi, M., Salavati-Niasari, M., 2021. Enhanced visible-light-driven photocatalytic performance for degradation of organic contaminants using PbWO4 nanostructure fabricated by a new, simple and green. Ultrason. Sonochem. 72, 105420.